# *Supplement of*
# Unprecedented strength of Hadley circulation in 2015-2016 impacts on $CO_2$ interhemispheric difference

Jorgen S. Frederiksen and Roger J. Francey

CSIRO Oceans and Atmosphere, Aspendale, Victoria, AUSTRALIA

*Correspondence to*: Jorgen S. Frederiksen (jorgen.frederiksen@csiro.au)

## SUPPLEMENTARY INFORMATION

### 1 Topographic Rossby waves during February 2015

As noted in the Introduction, the NASA (2016) OCO-2 $CO_2$ concentration in Figure 1b shows Rossby wave trains over the eastern Pacific and across South America on 17 February 2015. This episode is characteristic of other times of IH Rossby wave propagation during the boreal winter–spring, and particularly February, of 2015. The average 17 to 18 February 2015 streamfunction anomaly, from the thirty year 1981–2010 mean for the same period, is shown in Figure 1Sa for the Western Hemisphere ($0^o$W–$180^o$W) between $60^o$S and $60^o$N and at the $\sigma = 0.2582$ level. Here $\sigma = \frac{pressure}{surface\ pressure}$ and the corresponding pressure level is circa 260 hPa. We note that the phase lines broadly run from SW to NE between the Southern and Northern Hemispheres but are modulated by some smaller scale features. Moreover the dominant zonal wavenumber $m = 4$.

Indeed there are broad similarities between the streamfunction anomaly in Figure 1Sa and the streamfunction for the purely topographic Rossby waves in Figures 3a and b of Frederiksen and O'Kane (2005). For both the observations considered here and the ensemble of nonlinear simulations and statistical closure calculations the phase lines in the Western Hemisphere run SW to NE and the dominant wavenumber is 4. The dominant wavenumber 4 is also clearly seen in the energy spectra in Figure 2 of Frederiksen and O'Kane (2005). The SW to NW phase lines of pure topographic Rossby waves are also seen in the linear calculations in Figure 6 of Frederiksen (1982). In both the linear and nonlinear calculations the topographic Rossby waves are generated by the interaction of westerly winds with a conical mountain located at $30^o$ N (an idealized representation of the massive Himalayan orography) and for a situation where the near equatorial winds are westerly. For the observational results in Figure 1Sa, the near equatorial winds between $5^o$S and $5^o$N are westerly in the Western Hemisphere broadly above 400 hPa and easterly below (not shown).

Figure 1Sb shows the 300 hPa zonal wind anomaly corresponding to the average 17 to 18 February streamfunction anomaly in Figure 1Sa. Again the SW to NE phase lines are evident as is the dominant $m = 4$ wavenumber although the presence of smaller scale features associated with disturbances in the storm tracks (typically $m \sim 8-12$) is perhaps more evident. In Figures 2Sa and 2Sb we depict latitude pressure cross sections of the zonal wind anomalies for 17 to 18 February averaged between 120°W–140°W and 80°W–100°W respectively. We note that the anomaly is largely equivalent barotropic, as expected for topographic Rossby waves, and, by comparing the two panels, the SW to NW phase tilt is evident throughout the atmosphere. It can also be seen that the propagation across the equator into the Southern Hemisphere occurs primarily in the upper troposphere, particularly between 80°W–100°W where the mean westerly winds are weaker (not shown).

We have also plotted latitude pressure cross sections of anomalies of the vertical velocity in pressure coordinates, $\omega = dp/dt$ where $p$ is pressure, for 17 to 18 February averaged between 120°W–140°W and 80°W–100°W (not shown). These cross sections indicate that there is strong uplift in the Northern Hemisphere between 10°N and 30°N (negative $\omega$) and general descent south of that band to 30°S. The topographic Rossby wave train generated by westerly winds impinging on the Himalayas may interact with a small region of uplift focused over the Andes in Peru (not shown) when it crosses into the Southern Hemisphere. However, in addition it should be noted that the wave train occurs at a time of seasonal minimum in Southern Hemisphere $CO_2$.

## 2 Interhemispheric exchange of trace gases

Next, we consider the eddy and mean IH exchange of other trace gas species and their correlations with $CO_2$ and dynamical indices of transport. We focus on Feb-Apr for eddy transport and Jun-Aug for mean transport since these periods were the peaks for correlations of $CO_2$ IH difference with eddy and mean transport indices respectively. However, there are differences in the seasonal variability in the different trace gas species that are reflected in their transport and for that reason we also briefly mention the results for other time periods. We begin by further examining Mauna Loa minus Cape Grim (mlo–cgo) differences, between 1992-2016, in the routinely monitored CSIRO species $CH_4$, CO and $H_2$ in addition to $CO_2$ that were briefly considered in Frederiksen and Francey (FF16), as well as $N_2O$ (for 1993-2016). Thereafter we discuss mlo–cgo differences in $SF_6$ data sourced from the NOAA Halocarbons and other Atmospheric Trace Species Group (HATS) program from 1998 (NOAA, 2018).

### 2.1 Pacific westerly duct and eddy IH transport of CSIRO monitored trace gases

The IH exchange of the trace gas species $CH_4$, CO and $H_2$, in addition to $CO_2$, and the role of the Pacific westerly wind duct was also considered in FF16. In particular, the covariance, of the mlo–cgo difference in these routinely monitored CSIRO species with $u_{duct}$, is shown in Figure 5 of FF16. We recall that the $u_{duct}$ index is the average zonal wind in the region 5°N to 5°S, 140°W to 170°W at 300hPa. As noted in FF16, the extreme cases of Pacific westerly duct closure in 1997–98 and 2009–10 show up in the absence of seasonal IH exchange for $CH_4$ and CO as well as $CO_2$. The similar behaviour of detrended anomalies of mlo–cgo difference in $CH_4$, CO and $CO_2$ and their correlations with $u_{duct}$ is shown in Table 1S for Feb–Apr. We note the quite high correlations of $CH_4$ and CO with $CO_2$ ($r = 0.697$ and $r = 0.645$ respectively) and the significant anti–correlations of all these three species with $u_{duct}$ ($r = -0.448$, $r = -0.605$ and $r = -0.500$ respectively). In fact, for Mar-May the correlation between $CH_4$ and $CO_2$ is even larger at $r = 0.728$ (and with $u_{duct}$ it is $r = -0.474$) while between CO and $CO_2$ it is $r = 0.611$ (and with $u_{duct}$ it is $r = -0.507$). These results are of course consistent with Figure 5 of FF16 and are further evidence of similarities of IH transient eddy transport of these three gases. Table 1S also shows that the Feb-Apr correlation of $H_2$ with $CO_2$ and anti–correlation with $u_{duct}$ have smaller magnitudes ($r = 0.296$ and $r = -0.218$ respectively) although the Nov-Apr anti-correlation of $H_2$ with $u_{duct}$ is more comparable with $r = -0.463$. These results for anomalies are probably related to corresponding similarities and differences in the seasonal mean values (not shown) of these gases in Feb–Apr, as discussed below.

Anomalies in mlo–cgo differences in CSIRO monitored $N_2O$ are generally poorly correlated with those in $CO_2$ as shown for Feb-Apr and Jun-Aug in Tables 1S and 2S respectively (the maximum 3 month average correlation is $r = 0.274$ for Mar-May) and this is reflected in generally poor correlation with the dynamical indices shown in Tables 1S and 2S . This reflects the fact that natural exchanges with equatorial agriculture and oceans are the main sources (Ishijima et al., 2009), and the seasonal range in mlo-cgo difference is only around 0.2% of the mean $N_2O$ level, more than 10 times less than is the case for the other species.

## 2.2 Hadley circulation and mean IH transport of CSIRO monitored trace gases

We examine the role of the Hadley circulation on the mean transport of trace gases focusing on the boreal summer period of Jun–Aug. Table 2S shows the correlations between the detrended anomalies of mlo–cgo difference in $CH_4$, CO and $H_2$ with $CO_2$ and with the dynamical indices $\omega_P$ and $v_P$. Recall that $\omega_P$ is the 300 hPa vertical velocity in pressure coordinates, between $10^o$ N–$15^o$ N, and $v_P$ is the 200 hPa meridional wind, between $5^o$ N–$10^o$ N, and both are averaged over the 120°E–240°E Pacific sector. We note that the largest Jun-Aug correlation is between $H_2$ and $CO_2$ ($r = 0.680$) and the correlations between $CH_4$ and CO with $CO_2$ are considerably smaller ($r = 0.246$ and $r = 0.108$ respectively) while for Apr-Jun the latter correlations are more comparable at $r = 0.583$ and $r = 0.496$ respectively.

These correlations with $CO_2$ are also reflected in the respective correlations of the other trace gases with $\omega_P$ and $v_P$. We note from Table 2S that the Jun-Aug correlations of $H_2$ with $\omega_P$ and $v_P$ are $r = 0.427$ and $r = 0.442$ respectively which is slightly less than the corresponding correlations between $CO_2$ and the dynamical indices ($r = 0.522$ and $r = 0.539$ respectively) but considerably larger than for $CH_4$ and CO. For May-Jul the correlation of $H_2$ with $\omega_P$ is slightly larger with $r = 0.526$ .

Again, the different behaviour of the trace gas anomalies may be related to their different seasonal mean values; the seasonal mean IH difference for $H_2$ peaks in boreal summer while for $CH_4$ and CO it is relatively low with a minimum in August. The distribution and variability of surface exchange is different for each of the trace gases and there is potential for this to interact with the restricted extent and seasonal meandering of the regions of uplift to influence IH exchange of a species. For example, 70% of the global total $CH_4$ emissions are from mainly equatorial biogenic sources that include wetlands, rice agriculture, livestock, landfills, forests, oceans and termites (Denman et al., 2007) and CO emissions contain a significant contribution from $CH_4$ oxidation and from tropical biomass burning.

A more detailed examination of the inter–annual variation of the mlo–cgo difference in $H_2$ during boreal summer is presented in Figure 3S. It shows the detrended $H_2$ data in comparison with the corresponding $CO_2$ data and with the $\omega_P$ and $v_P$ indices. First we note that the detrended $CO_2$ data in the top panel has very similar inter–annual variation to the FF–adjusted $C^{*}_{\text{mlo-cgo}}$ in Figure 6b. We also see that the qualitative behaviour of $H_2$ mirrors many aspects of $CO_2$, as expected from the correlations in Table 2S. In particular, the increase in the IH difference of $H_2$ in 2010 is even more pronounced than for $CO_2$. For $CO_2$ and for $H_2$ there is a steady reduction in the IH difference from around 2013 leading to a local minimum in 2016. In both of these respects these gases broadly follow the changes in the Hadley circulation including the strengthening during 2015–2016. Vertical lines in Figure 3S indicate other times between 1992 and 2016 when transitions occur in both these trace gases and in the Hadley circulation characterized by $\omega_P$ and $v_P$.

Surface exchanges of $H_2$ have similarities to those of $CO_2$ in that they occur mostly at mid–northern latitudes and are mainly due to emissions from Fossil Fuel combustion. However $H_2$ also has mid–northern latitude photochemical sources peaking in August (Price et al., 2007). These boreal summer sources are almost offset by a combined soil and hydroxyl sink, but the overall interhemispheric partial pressure difference is boosted by a significant reduction in the Southern Hemisphere photochemical source at that time. For both species, the most northern excursions of the inter–tropical convergence zone that occurs at Pacific latitudes encounter increasing concentrations of both gases.

As noted above, anomalies in mlo–cgo differences in $N_2O$ are poorly correlated with those in $CO_2$ and in dynamical indices (Tables 1S and 2S). Indeed the 3 month average anti-correlation with $u_{duct}$ that has the largest magnitude is $r = -0.133$ for Mar-May and the largest correlations with $\omega_P$ is $r = 0.359$ for Apr-Jun and with $v_P$ is $r = 0.350$ for May-Jul.

## 2.3 Interhemispheric exchange of $SF_6$

In the case of SF6 we have analysed the mlo–cgo difference in available NOAA HATS data from 1998 to 2012 when cgo HATS measurements ceased. Correlations of detrended anomalies in IH differences in $SF_6$ with those in $CO_2$ are as follows: the Feb–Apr correlation is $r = 0.619$, the Mar-May correlation is $= 0.722$, the Apr-Jun correlation is $r = 0.595$, the May–Jul correlation is $r = 0.303$ and the Jun–Aug correlation is $r = 0.223$. The corresponding correlations with dynamical indices are as follows: for Feb–Apr the correlation with $u_{duct}$ is $r = -0.617$, the May–Jul correlations with $\omega_P$ is $r = 0.465$, the Jun–Aug correlation with $\omega_P$ is $r = 0.433$, the May–Jul correlation with $v_P$ is $r = 0.517$ and the Jun–Aug correlation with $v_P$ is $r = 0.385$. We note that $SF_6$ has an anti-correlation with $u_{duct}$ for Feb-Apr that has larger magnitude than for $CO_2$ and even $CH_4$. Thus, there is again a significant influence of the Pacific westerly duct, in late boreal winter and spring, and of the Hadley circulation, in boreal summer and late spring, as measured by these indices, on the mlo–cgo differences of $SF_6$; these $SF_6$ differences exhibit a similar step change in 2009-2010 as shown for $CO_2$ in Figures 2 and 6.

## 2.4 Implications for constaining terrestrial biosphere exchange

The sign and strength of zonal winds in the Pacific westerly duct ($u_{duct}$) are correlated with corresponding changes in near-equatorial transient kinetic energy (Fig. 6, Frederiksen and Webster 1988) resulting in changes in the mixing of trace gases. This effect may not be adequately represented in the parameterizations used in atmospheric transport models. Model determinations of short term variations in the Hadley circulation exchange are also susceptible to uncertainties in representations of the equatorial convective dynamics (Lintner et al. 2004). By identifying spatial changes due to transport and providing empirical indices that describe short-term variations in both Pacific westerly duct and Hadley transfers there is potential to improve atmospheric constraints on Dynamic Vegetation modelling.

*Acknowledgements.* The dynamics contributions were prepared using data and software from the NOAA/ESRL Physical Sciences Division web site: http://www.esrl.noaa.gov/psd/. The trace gas data for CSIRO monitored species $CO_2$, $CH_4$, CO, $H_2$ and $N_2O$ and the NOAA monitored $SF_6$ are available from the World Data Centre for Greenhouse Gases website:
https://ds.data.jma.go.jp/gmd/wdcgg/cgi-bin/wdcgg/catalogue.cgi

### References

1. Denman, K. L., Brasseur, G., Chidthaisong, A., Ciais, P., Cox, P. M., Dickinson, R. E., Hauglustaine, D., Heinze, C., Holland, E., Jacob, D., Lohmann, U., Ramachandran, S., da Silva Dias, P. L., Wofsy, S. C., & Zhang, X.: Couplings Between Changes in the Climate System and Biogeochemistry. In: *Climate Change 2007: The Physical Science Basis. Contribution of Working Group I to the Fourth Assessment Report of the Intergovernmental Panel on Climate Change* [Solomon, S., Qin, D., Manning, M., Chen, Z., Marquis, M., Averyt, K.B., Tignor, M. & Miller, H.L. (eds.)]. Cambridge University Press, Cambridge, United Kingdom and New York, NY, USA, 2007.
2. Francey, R. J., & Frederiksen, J. S.: The 2009–2010 step in atmospheric $CO_2$ interhemispheric difference, Biogeosciences, 13, 873–885, doi:10.5194/bg-13-873-2016, 2016.
3. Frederiksen, J. S.: Eastward and westward flows over topography in nonlinear and linear barotropic models, J. Atmos. Sci., 39, 2477–2489, 1982.
4. Frederiksen, J. S. & O'Kane, T. J.: Inhomogeneous closure and statistical mechanics for Rossby wave turbulence over topography, J. Fluid Mech., 539**,** 137–165, 2005.
5. Frederiksen, J. S. & Webster, P. J.: Alternative theories of atmospheric teleconnections and low-frequency fluctuations, Rev. Geophys., 26, 459–494, 1988.
6. Ishijima, K., Nakazawa, T., & Aoki, S.: Variations of atmospheric nitrous oxide concentration in the northern and western Pacific, Tellus B, 61:2, 408–415, doi: 10.1111/j.1600-0889.2008.00406.x, 2009.
7. Lintner, B. R., Gilliland, A. B., & Fung, I. Y.: Mechanisms of convection-induced modulation of passive tracer interhemispheric transport interannual variability, J. Geophys. Res., 109, D13102, doi:10.1029/2003JD004306, 2004.

8. NASA: Following carbon dioxide through the atmosphere, 2016. https://www.nasa.gov/feature/goddard/2016/eye-popping-view-of-co2-critical-step-for-carbon-cycle-science
9. Price, H., Jaegle´, L., Rice, A., Quay, P., Novelli, P. C., & Gammon, R.: Global budget of molecular hydrogen and its deuterium content: Constraints from ground station, cruise, and aircraft observations, J. Geophys. Res., 112, D22108, doi:10.1029/2006JD008152, 2007.
10. NOAA, 2018. http://www.esrl.noaa.gov/gmd/

**Tables**

Table 1S: Correlations $(r)$ between the detrended mlo–cgo gas anomalies for $CO_2$, $CH_4$, CO and $H_2$ with $CO_2$ and $u_{duct}$ index of transient transport averaged between Feb–Apr for 1992–2016. Also shown are corresponding correlations for $N_2O$ and 1993-2016 and for $SF_6$ and 1998-2012.

| Gas | $CO_2$ | $u_{duct}$ |
|---|---|---|
| $CO_2$ | $r$ = 1.0 | $r$ = –0.500 |
| $CH_4$ | $r$ = 0.697 | $r$ = –0.448 |
| $CO$ | $r$ = 0.645 | $r$ = –0.605 |
| $H_2$ | $r$ = 0.296 | $r$ = –0.218 |
| $N_2O$ | $r$ = 0.215 | $r$ = –0.088 |
| $SF_6$ | $r$ = 0.619 | $r$ = –0.617 |

Table 2S: Correlations $(r)$ between the detrended mlo–cgo gas anomalies for $CO_2$, $CH_4$, CO and $H_2$ with $CO_2$ and indices of mean transport, $\omega_P$ and $v_P$ averaged between Jun–Aug for 1992–2016. Also shown are corresponding correlations for $N_2O$ and 1993-2016 and for $SF_6$ and 1998-2012.

| Gas | $CO_2$ | $\omega_P$ | $v_P$ |
|---|---|---|---|
| $CO_2$ | $r$ = 1.0 | $r$ = 0.520 | $r$ = 0.534 |
| $CH_4$ | $r$ = 0.246 | $r$ = 0.195 | $r$ = 0.250 |
| $CO$ | $r$ = 0.108 | $r$ = 0.205 | $r$ = 0.236 |
| $H_2$ | $r$ = 0.680 | $r$ = 0.427 | $r$ = 0.442 |
| $N_2O$ | $r$ = –0.010 | $r$ = 0.290 | $r$ = 0.266 |
| $SF_6$ | $r$ = 0.223 | $r$ = 0.433 | $r$ = 0.385 |

**Figures**

Figure 1S

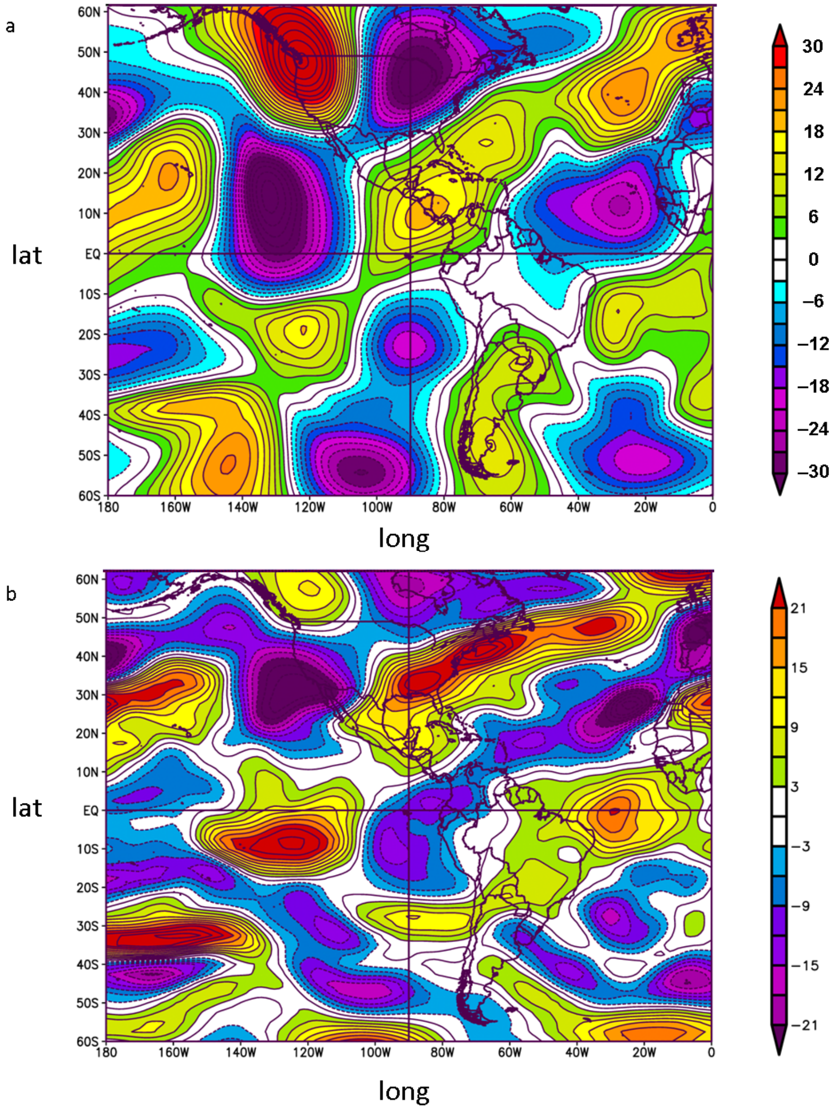


Figure 1S: The average 17 to 18 February 2015 (a) streamfunction anomaly at $\sigma = 0.2582$ in kms$^{-1}$ and (b) zonal wind anomaly at 300 hPa in ms$^{-1}$ where the anomalies are with respect to the thirty year 1981–2010 mean for the same period.

Figure 2S

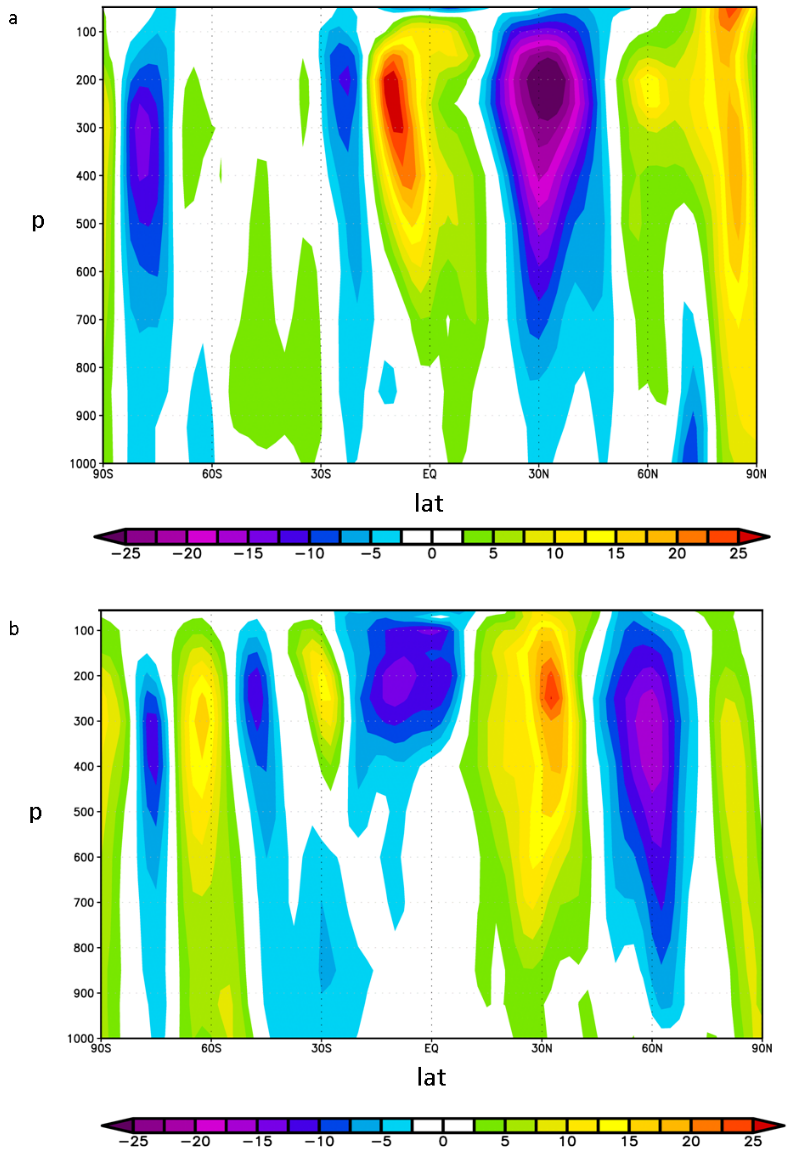


Figure 2S: Latitude pressure cross sections of zonal wind anomalies in $ms^{-1}$ for 17 to 18 February 2015 averaged between (a) 120°W–140°W and (b) 80°W–100°W.

Figure 3S

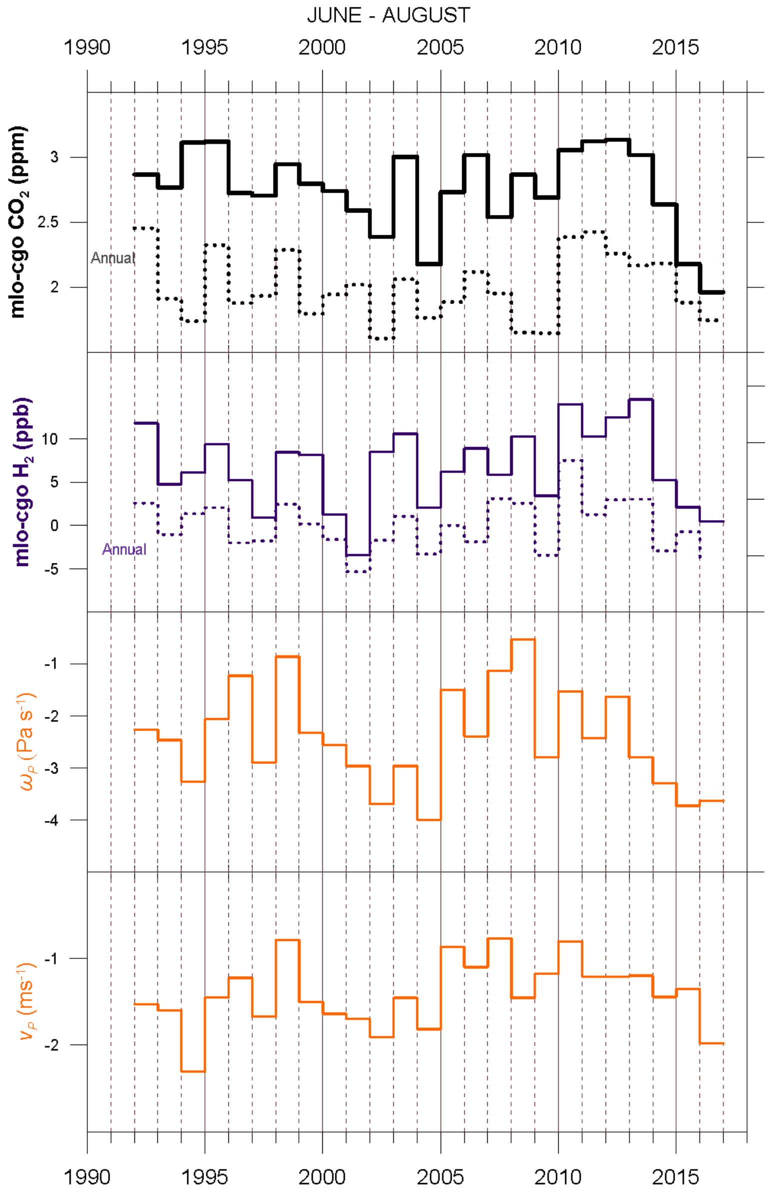


Figure 3S: Time series of June–August and Annual averages of detrended mlo–cgo differences in $CO_2$ and $H_2$ and June–August average dynamical indices $\omega_P$ and $v_P$ .